Three-dimensional numerical analysis of active flow control for rigid wingsails using co-flow jet

7th International Conference on Innovation in High Performance Sailing Yachts and Wind Assisted Ships.
InnovSail 2026, Gothenburg, Sweden, 3-5 June 2026.

Three-dimensional numerical analysis of active flow control for rigid wingsails using co-flow jet

Heng Zhu
Chalmers University of Technology, Department of Mechanics and Maritime Sciences, Division of Marine Technology, Gothenburg 41296, Sweden. Corresponding author: heng.zhu@chalmers.se

Petter Engström
Chalmers University of Technology, Department of Mechanics and Maritime Sciences, Division of Marine Technology, Gothenburg 41296, Sweden.

Kewei Xu
Department of Mechanical Engineering, University of Maine, Orono 04469, ME, USA.

Rickard Bensow
Chalmers University of Technology, Department of Mechanics and Maritime Sciences, Division of Marine Technology, Gothenburg 41296, Sweden.

Abstract

Flow separation over rigid wingsails at moderate to high angles of attack limits aerodynamic efficiency and increases load fluctuations, which constrains their performance in wind-assisted ship propulsion (WASP) systems. The objective of this study is to evaluate the effectiveness of active flow control using a co-flow jet (CFJ) in enhancing the aerodynamic performance of rigid wingsails and to clarify the associated three-dimensional flow mechanisms. Three-dimensional unsteady CFD simulations are conducted for two sectional profiles, a symmetric NACA 0015 and a cambered crescent-shaped D2R8, under controlled and baseline conditions. The CFJ is implemented through jet injection and suction to modify boundary-layer development and separation behavior. The results show that CFJ significantly alters the suction-side separation pattern, delays stall onset, and improves pressure recovery. The controlled cases exhibit increased lift and thrust coefficients compared with the baseline configurations. The enhancement is attributed to boundary-layer energization and circulation redistribution induced by the jet–shear-layer interaction. The outcomes indicate that CFJ control can substantially modify separation behavior in rigid wingsails and improve propulsive performance under the examined conditions.

Keywords: active flow control; CFD; co-flow jet; wind-assisted ship propulsion; wingsail.

NOMENCLATURE

A_{ref}	Reference area, $L_c \cdot L_s$ [m^2]
A_j	Jet slot area [m^2]
C_D	Drag coefficient [-]
$C_{D,surface}$	Surface-integrated drag coefficient [-]
C_L	Lift coefficient [-]
$C_{L,surface}$	Surface-integrated lift coefficient [-]
C_μ	Jet momentum coefficient [-]
F_D	Drag force [N]
F_L	Lift force [N]

$\mathbf{F}$	Total aerodynamic force $[\mathrm{N}]$
$\mathbf{F}_{\mathrm{surface}}$	Surface-integrated aerodynamic force $[\mathrm{N}]$
L_c	Chord length $[\mathrm{m}]$
L_s	Spanwise length $[\mathrm{m}]$
$\dot{m}$	Jet mass flow rate $[\mathrm{kg \cdot s^{-1}}]$
$\mathbf{n}$	Outward unit normal vector [-]
$\mathbf{n}_{\mathrm{j}}$	Outward unit normal vector at jet slot [-]
N_{layer}	Number of prism layers $[\mathrm{m}]$
p	Relative pressure $[\mathrm{Pa}]$
p_j	Jet pressure [Pa]
Q	Q-criterion $[\mathrm{s^{-2}}]$
Re	Reynolds number [-]
T	Time [s]
$t_{first\ layer}$	Thickness of the near-wall prism layer $[\mathrm{m}]$
t_{total}	Total thickness of prism layer $[\mathrm{m}]$
V_∞	Freestream velocity magnitude $[\mathrm{m}/s]$
$\mathbf{V}_{\mathrm{j}}$	Jet velocity at injection slot $[\mathrm{m}/s]$
$\mathbf{x}$	Freestream direction unit vector $[\mathrm{m}]$
$\mathbf{y}$	Crossflow direction unit vector $[\mathrm{m}]$
y^+	Dimensionless wall distance [-]
α	Angle of attack [°]
ρ_∞	Freestream density $[\mathrm{kg \cdot m^{-3}}]$
$\boldsymbol{\tau}$	Wall shear stress $[\mathrm{Pa}]$

AFC	Active Flow Control
CFD	Computational Fluid Dynamics
CFJ	Co-flow Jet
DES	Detached Eddy Simulation
EFD	Experimental Fluid Dynamics
LES	Large Eddy Simulation
URANS	Unsteady Reynolds-Averaged Navier–Stokes
WASP	Wind-Assisted Ship Propulsion

1. Introduction

Wind-assisted ship propulsion (WASP) has re-emerged as a promising approach to significantly reduce fuel consumption and emissions in the maritime sector (Huang & Souppez, 2025; Lu & Ringsberg, 2020; Petković *et al.*, 2021; Thies & Fakiolas, 2022). Modern WASP systems encompass a range of technologies, including rigid wingsails, soft sails, rotor sails, and kites, which can provide auxiliary thrust to marine vessels and improve overall energy efficiency (Khan *et al.*, 2021; Thies & Fakiolas, 2022). These passive and semi-active systems have demonstrated potential for double-digit fuel savings and emissions reductions, making them attractive for meeting emerging regulatory targets in shipping decarbonization. Among WASP technologies, rigid wingsail configurations are particularly effective in generating propulsive force due to their high lift and low drag characteristics, especially under moderate to high apparent wind angles (θ_{AW}), making them suitable for both yachts and large vessels (Li *et al.*, 2017; Ouchi *et al.*, 2011; Zhu *et al.*, 2023b). Wingsails with cambered profiles, such as crescent-shaped sections, have been shown to achieve greater thrust than conventional symmetric airfoils (Souppez & Viola, 2024; Zeng *et al.*, 2024a; Zhu *et al.*, 2023b). However, cambered profiles inherently exhibit strong adverse pressure gradients and are prone to early flow separation and stall, particularly at high angles of attack (α) encountered in board-reach sailing conditions (Souppez *et al.*, 2022; Zhu *et al.*, 2023b). Such separation significantly degrades aerodynamic efficiency and induces unsteady loading, limiting the potential thrust gain of these profiles.

In the meantime, active flow control (AFC) techniques have been widely applied in aerodynamic systems to mitigate separation, enhance lift, and delay stall (Balaji & Wessley, 2023; Jahanmiri, 2010). In aircraft applications, devices such as synthetic jets and co-flow jets (CFJ) have been investigated extensively to manipulate boundary layer momentum and suppress adverse separation (Ding *et al.*, 2025; Xu & Zha, 2021, 2023b). These control strategies leverage phenomena such as the Coandă effect to energize near-wall flow and improve surface adherence, resulting in improved aerodynamic performance. It is worth noting that these jet-related technologies have seen rapid development in aerospace and related fields over the past decades (Ho *et al.*, 2024; Zha *et al.*, 2007). Recent work regarding synthetic jet and CFJ actuators has explored advanced configurations such as multi-orifice designs and actuator arrays to improve coverage and control authority in turbulent boundary layers (Pasa *et al.*, 2026). It has been indicated that key parameters such as jet momentum coefficient (C_μ) and slot geometry have been shown to strongly influence control effectiveness (Su *et al.*, 2023; Wang *et al.*, 2022). These developments highlight the growing breadth of AFC techniques beyond traditional slot blowing, motivating their adaptation to other airfoil-related fields.

In marine applications, related concepts such as suction sails employ continuous boundary-layer suction over extended surface regions to delay separation and stabilize the flow (Charrier *et al.*, 1985; Du *et al.*, 2025). For instance, Du *et al.* (2026) quantified the influence of blowing momentum coefficient and slot configuration on aerodynamic efficiency, showing that optimized actuation strategies can yield substantial thrust augmentation. While suction-based approaches primarily rely on the extraction of low-momentum fluid, the CFJ method combines localized momentum injection with downstream suction in a closed-loop configuration. By introducing additional streamwise momentum into the near-wall region, CFJ actively redistributes circulation and modifies separation topology rather than solely suppressing boundary-layer growth. Building upon established AFC studies from aeroengineering, several studies have explored the application of CFJ and related momentum-injection strategies to wingsails. For instance, Ren *et al.* (2026) have explored CFJ concepts for windsails, demonstrating their potential for enhanced thrust generation and active flow control. Engström *et al.* (2026a); Engström *et al.* (2025) demonstrated that CFJ implementation on symmetric wingsail sections can significantly enhance thrust coefficients and delay stall under high-angle operating conditions. Subsequent investigations extended the concept to cambered crescent-type airfoils, reporting notable improvements in lift-to-drag ratio and net propulsive performance through optimized jet momentum coefficients and slot configurations (Engström *et al.*, 2026b). Similarly, Cairns *et al.* (2021) demonstrated that steady blowing-based active flow control applied to rigid wingsails can significantly delay stall and improve thrust performance under high apparent wind angles, primarily through enhanced boundary-layer momentum and separation suppression. However, most of the existing AFC investigations for wingsail applications remain limited to two-dimensional simulations, while this limitation becomes particularly significant because separation suppression in cambered profiles at high Reynolds numbers (Re) is inherently three-dimensional (Xu *et al.*, 2025; Zeng *et al.*, 2024b; Zhang *et al.*, 2024; Zhu *et al.*, 2024b). While such approaches are suitable for comparative performance evaluation and preliminary design screening, they inherently suppress or model out key three-dimensional flow structures, including spanwise vortex interactions, tip-induced effects, and large-scale unsteady separation dynamics.

From a methodological perspective, the state of the art in wingsail aerodynamics has been dominated by performance-oriented studies. Most investigations focus on the evaluation of lift, drag, and thrust coefficients under various apparent wind angles and operational conditions, often relying on steady Reynolds-averaged Navier–Stokes (URANS) simulations (e.g., Persson *et al.* (2019); Zeng *et al.* (2023); Zhu *et al.* (2023b)) or wind tunnel measurements (e.g., Giovannetti *et al.* (2022); Zhang *et al.* (2022); Zhu *et al.* (2023a)). Such approaches provide valuable insights into overall aerodynamic efficiency and installation strategies but are primarily geared toward integrated performance assessment rather than detailed flow mechanisms. High-fidelity investigations of the underlying flow mechanisms remain comparatively limited. A small number of studies have employed large eddy simulation (LES) (e.g., Zeng *et al.* (2024a)), detached eddy simulation (DES) (e.g., Zhu *et al.* (2024b)), or advanced experimental techniques such as particle image velocimetry (PIV) (e.g., Souppez and Viola (2024)) to resolve separation dynamics, vortex shedding, and three-dimensional coherent structures associated with cambered wingsail sections. These studies have revealed complex unsteady flow features, including large-scale separation bubbles and spanwise vortex interactions, which are not fully captured by conventional URANS approaches. This imbalance between performance evaluation and mechanism-oriented research becomes especially critical in the context of AFC, because the design, parameter selection, and optimization of AFC systems are inherently dependent on a precise understanding of separation onset, boundary-layer momentum redistribution, and unsteady vortex dynamics (Jahanmiri, 2010). Without resolving the dominant flow structures and their interaction with control inputs, the predictive capability of AFC simulations remains uncertain. Therefore, advancing the aerodynamic understanding of controlled cambered wingsail flows requires not only performance comparison but also physics-based analysis supported by higher-fidelity modeling.

In this context, the objective of this study is to advance the understanding of AFC for cambered wingsail configurations through three-dimensional analysis. Building upon previous two-dimensional investigations (Engström *et al.*, 2025, 2026b), this work evaluates the aerodynamic performance enhancement induced by a CFJ system applied to both a symmetric NACA 0015 airfoil and a cambered crescent-shaped D2R8 profile. The primary focus is to introduce three-dimensional URANS simulations in order to characterize spanwise flow development, separation topology, and coherent vortex structures that cannot be captured in two-dimensional frameworks. Particular attention is given to how three-dimensional flow features influence the effectiveness of momentum injection and overall thrust generation. In addition, selected cases are further examined using LES to provide physics-resolving insights into the interaction between CFJ actuation and unsteady separation dynamics. Through these approaches, the study aims to bridge performance-oriented AFC evaluation with mechanism-based aerodynamic analysis for controlled wingsail flows.

It should be noted that, in the context of wind-assisted ship propulsion, different from fixed-angle aerodynamic devices, wingsails can be actively trimmed with a large range of angles of attack, but in the present study, the focus is on conditions where the highest lift force coefficient is generated, *i.e.*, highly loaded side-wind conditions. Besides, the CFJ system is an AFC approach, requiring additional energy input to drive the injection and suction processes, so any net propulsive benefit in practical applications must account for the power consumption of the jet system. However, the present study focuses on the aerodynamic mechanisms induced by CFJ under controlled conditions, rather than a full system-level performance assessment. Thus, a quantitative evaluation of the net energy balance, including the jet power consumption, is beyond the scope of this work and will be addressed in future studies.

2. Methods

2.1 Design and Active Flow Control Configuration

Two sectional profiles are considered in the present study: a symmetric NACA 0015 airfoil and a cambered crescent-shaped profile (D2R8) (Zhu *et al.*, 2024b). The NACA 0015 airfoil serves as a canonical reference geometry, while the crescent-shaped profile represents a high-camber configuration developed for rigid wingsail applications. The crescent-shaped profile baseline is constructed from circular arcs and is symmetric with respect to the half-chord line, enabling operation under both port and starboard wind conditions (Zhu *et al.*, 2023b). As mentioned in Section 1, owing to its large suction-side curvature and blunt leading and trailing edges, the crescent profile generates high lift at moderate angles of attack ($\sim 20°$) but is prone to strong flow separation (Zhu *et al.*, 2024b; Zhu *et al.*, 2023b). This characteristic makes it a suitable candidate for evaluating the effectiveness of active flow control. All sectional dimensions and geometric parameters of the crescent profile are consistent with those reported in previous studies (Engström *et al.*, 2026b; Zhu *et al.*, 2024b; Zhu *et al.*, 2023b), ensuring comparability of the present results with earlier investigations.

Wingsails with NACA 0015 and crescent-shaped D2R8 are simulated under $\alpha = 15°$ (Engström *et al.*, 2025) and $20°$ (Zhu, 2024; Zhu *et al.*, 2024b), respectively, as these values of α are close to the critical angle of attack with the highest lift force coefficient (C_L). For both profiles, the chord length (L_c) is 0.4 m, and the spanwise length (L_s) is 0.1 m, meaning that the aspect ratio is 0.25. The free-stream velocity (V_∞) is 25 m/s, which corresponds to $Re = 7.6 \times 10^5$.

For the NACA 0015 airfoil, the CFJ configuration follows the design framework proposed by Engström *et al.* (2026a); Engström *et al.* (2025), ensuring consistency with previously validated active flow control implementations for wingsail sections. Similarly, for the D2R8 profile, a bi-directional symmetric co-flow jet (CFJ) configuration is also implemented (Engström *et al.*, 2026b), as illustrated in **Figure 1**. The system consists of injection slots located near the leading edge and suction slots positioned closer to the trailing edge. The injection and suction slots are connected internally through a micro-compressor, forming a circulation system.

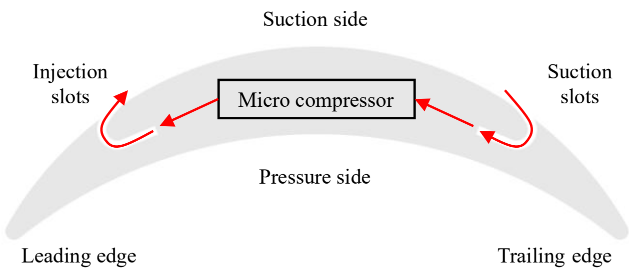

Figure 1. Schematics of a crescent-shaped D2R8 profile with a bi-directional symmetric CFJ design.

The CFJ introduces high-momentum fluid into the near-wall region on the suction side while extracting low-momentum fluid downstream. In this manner, additional streamwise momentum is supplied to the boundary layer, thereby mitigating separation under strong adverse pressure gradients. At the sectional level, the configuration operates as a zero-net-mass-flux system, as the injected mass flow rate is balanced by the suction mass flow rate.

C_μ of the CFJ is characterized by

$$C_\mu = \frac{\dot{m}V_j}{\frac{1}{2}\rho_\infty V_\infty^2 A_{ref}}, \tag{1}$$

where $\dot{m}$ is the jet mass flow rate, V_j is the jet velocity at the injection slot, ρ_∞ denotes the freestream density, and $A_{ref} = L_c \cdot L_s$ is the chord-based reference area. In the present study, a fixed value of $C_\mu = 0.3$ is adopted to evaluate the performance enhancement under separated flow conditions (Engström *et al.*, 2025).

2.2 Computational Domain and Boundary Conditions

A three-dimensional computational domain is constructed to simulate the aerodynamic behavior of the wingsail sections under uniform incoming flow. The global Cartesian coordinate system is defined with the X-axis aligned with the freestream direction, the Y-axis normal to the freestream in the sectional plane, i.e., the crossflow direction, and the Z-axis corresponding to the spanwise direction. The origin is located at the leading edge of the wingsail at the bottom panel.

As illustrated in **Figure 2**, the far-field domain is defined as a circular region with a diameter of $30L_c$ (Engström *et al.*, 2025). This size ensures negligible blockage effects and minimizes artificial reflection of disturbances from the outer boundary.

The spanwise direction is modeled using periodic boundary conditions, representing a representative spanwise segment of an infinitely extended wingsail. Velocity inlet boundary condition is specified at the upstream semi-circle and pressure outlet is applied on the downstream semi-circle. At the velocity inlet boundary, a uniform velocity inlet condition is prescribed with V_∞. As mentioned in Section 1, based on the scope of this study, the inlet flow is prescribed with a relatively low turbulence intensity, and does not aim to reproduce a fully developed atmospheric boundary layer. This setup is adopted to isolate the effects of CFJ-induced flow control under controlled conditions. All solid surfaces of the airfoil are treated as no-slip walls. For the CFJ configuration, the injection and suction slots are modeled as mass flow inlets with prescribed mass flow rate corresponding to the desired C_μ. The jet direction is aligned tangentially to the local surface to ensure co-flow injection along the suction side. The absolute values of the mass flow at the injection and suction slots are the same.

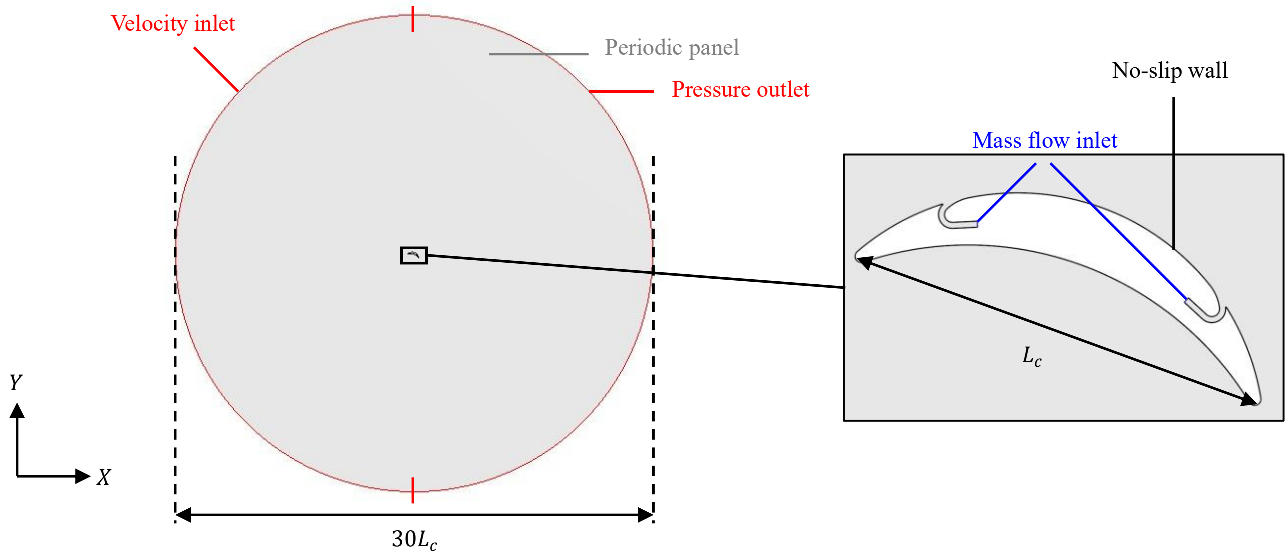

Figure 2. Computational domain and boundary condition. Crescent-shaped D2R8 profile with CFJ.

2.3 Turbulence Model and Numerical Solver

All simulations are performed using the commercial CFD software Simcenter STAR-CCM+ (Siemens PLM Software, 2021). The governing equations are solved within the framework of URANS formulation for the majority of the cases considered in this study. The blended wall treatment approach (Workinn, 2021) is applied to the RANS equations, offering the advantage of accommodating complex geometries with varying local flow characteristics.

Turbulence effects are modeled using the two-equation k–ω shear stress transport (SST) model (Menter, 1993), which combines the robustness of the k–ω formulation in the near-wall region with the free-stream independence of the k–ε model in the outer flow. The SST model is selected due to its demonstrated capability in predicting adverse pressure gradient flows and separation phenomena, which are central to the present investigation. Previous studies have indicated that for crescent-shaped profiles, the flow field is sensitive to Re within the range from 10^5 to 10^6 (Zhu, 2024). Hence, to account for laminar-to-turbulent transition effects, the γ–Re_θ transition model (Langtry & Menter, 2009) is employed. This model introduces transport equations for intermittency and transition onset momentum thickness Reynolds number, enabling improved prediction of transitional separation behavior.

An implicit unsteady time integration scheme is adopted for all simulations. The pressure–velocity coupling is handled using a segregated flow solver, in which the momentum and continuity equations are solved sequentially within each time step. This approach ensures numerical stability while maintaining computational efficiency for three-dimensional simulations.

A compressible flow formulation is employed to solve the governing equations, including the total energy equation. The segregated fluid enthalpy model is used, where the total energy is solved in terms of enthalpy and the temperature is subsequently computed via the equation of state. Although the present simulations operate at low Mach numbers, the compressible formulation provides consistent treatment of energy transport and density variations within the numerical framework.

2.4 Discretization Schemes and Numerical Mesh

The governing equations are discretized using a finite volume method (FVM) on an unstructured polyhedral mesh. Convective fluxes are discretized using a second-order upwind scheme, while diffusive terms are treated with second-order central differencing. Temporal discretization is performed using a second-order implicit unsteady scheme.

A fixed physical time step of 1×10^{-5} s is employed for all unsteady simulations. The Courant–Friedrichs–Lewy (CFL) number is strictly maintained below 10 throughout the computational domain and remains below 1 in the majority of flow regions. The reported value refers to the maximum CFL number in the computational domain; the local CFL number in the near-wall prism-layer region and suction-side boundary-layer region is lower than this maximum value. Each physical time step consists of 15 inner iterations to ensure convergence of the segregated solver within the time advancement procedure.

The numerical mesh consists predominantly of polyhedral cells with targeted local refinement near the airfoil surface, CFJ slots, and wake region, as illustrated in **Figure 3**. In the wake, a refinement zone extending approximately $4L_c$ downstream of the trailing edge is introduced to resolve vortex shedding and shear layer development (Engström *et al.*, 2025). The wake refinement spans an angular sector of approximately 0.1 rad in the sectional plane to adequately capture separation-induced coherent structures.

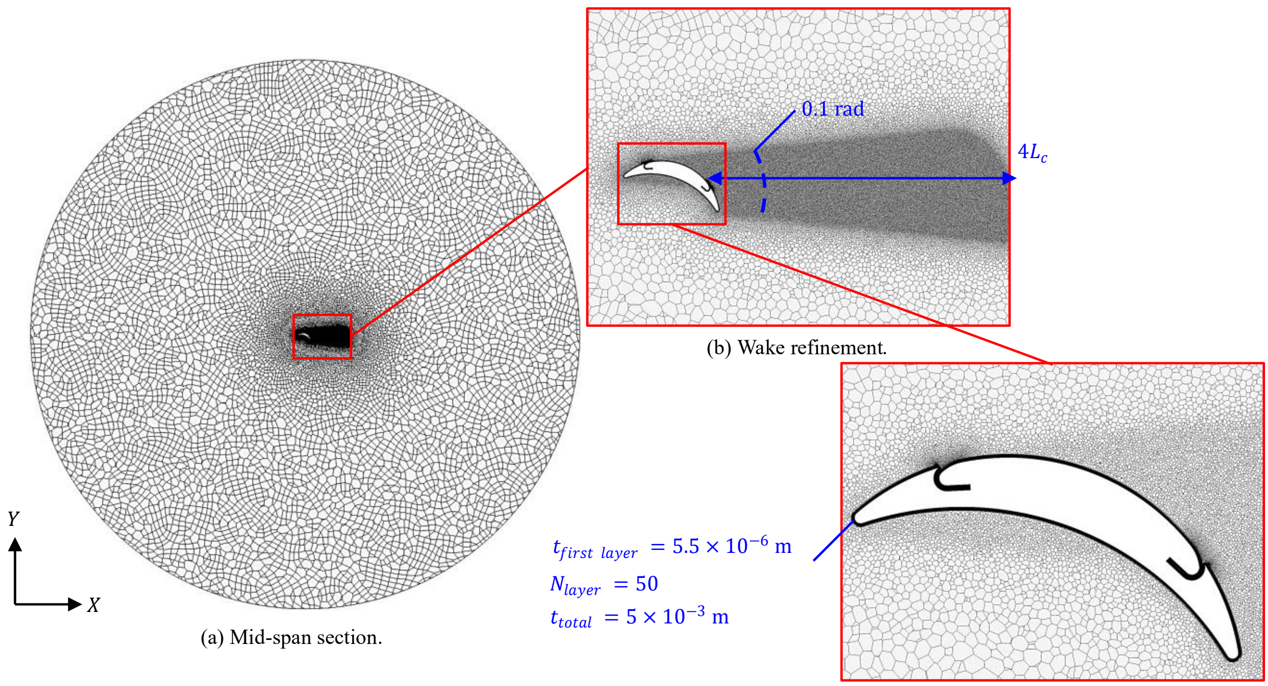

(a) Mid-span section.
(b) Wake refinement.
(c) Boundary layer refinement.

Figure 3. Numerical mesh. Crescent-shaped D2R8 profile with CFJ.

Near-wall resolution is achieved using prism-layer refinement along the airfoil surface. The first-layer thickness is $5.5 \times 10^{-6}\mathrm{m}$, with 50 prism layers and a total boundary-layer thickness of 5×10^{-3} m. The resulting dimensionless wall distance satisfies $y^+ < 5$ over the entire surface and remains below unity over most of the wall area, typically on the order of 10^{-1}. This resolution ensures proper near-wall treatment for the k–ω SST turbulence model and transition modeling.

Mesh refinement strategies for two-dimensional CFJ simulations have previously been verified by Engström *et al.* (2025), while three-dimensional mesh sensitivity for the baseline crescent-shaped wingsail without AFC has been established by Zhu *et al.* (2023b). Given the already highly refined mesh employed in the present study, a full multi-level mesh convergence study is not repeated. Instead, four refinement levels are tested to confirm negligible variation in integrated aerodynamic coefficients. As shown in **Figure 4**, the differences in the time-averaged surface-integrated lift and drag coefficients ($\langle C_{L,surface} \rangle$ and $\langle C_{D,surface} \rangle$) between the medium-fine and fine meshes are within approximately 2%, indicating satisfactory grid convergence for the quantities of interest. To ensure the quality of resolution, the fine mesh is selected for subsequent simulations. The selected mesh is subsequently used for both URANS and LES simulations. Owing to the high near-wall and wake resolution, the same mesh is adopted for LES cases without further refinement. It should be noted that, strictly speaking, the instantaneous resolved flow field, especially in LES, cannot be fully independent of the mesh because progressively smaller turbulent structures are resolved as the grid is refined. Therefore, the present assessment focuses on the convergence of integral quantities, namely the time-averaged lift and drag coefficients, rather than claiming complete mesh independence of the flow field.

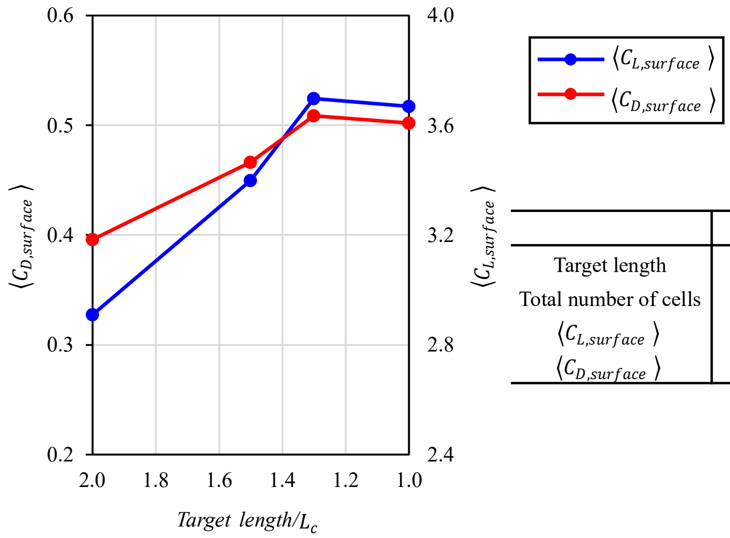

	Coarse	Medium coarse	Medium fine	Fine
Target length	$2L_c$	$1.5L_c$	$1.3L_c$	L_c
Total number of cells	5,103,597	8,932,103	13,203,636	18,088,994
$\langle C_{L,surface} \rangle$	2.910	3.398	3.698	3.668
$\langle C_{D,surface} \rangle$	0.396	0.466	0.509	0.502

Figure 4. Mesh sensitivity verification. Crescent-shaped D2R8 profile with CFJ.

2.5 Wind load analysis

The aerodynamic loads acting on the wingsail sections are obtained by surface integration of pressure and viscous shear stresses over the airfoil surface. The total force vector ($\mathbf{F}_{\mathrm{surface}}$) is computed as

$$\mathbf{F}_{\mathrm{surface}} = \oiint_A (-p\mathbf{n} + \boldsymbol{\tau})\mathrm{d}A\,, \tag{2}$$

where p is the relative pressure, $\boldsymbol{\tau}$ is the shear stress, and $\mathbf{n}$ is the outward surface normal vector. The resulting force components are projected onto the freestream-aligned coordinate system to obtain surface-integrated lift force ($F_{L,surface}$) and surface-integrated drag force ($F_{D,surface}$).

For CFJ cases, the total lift and drag are calculated by accounting for the reaction forces associated with the injection and suction jets (Engström *et al.*, 2025; Zha *et al.*, 2007). The total wind loads ($\mathbf{F}$) are then expressed as

$$\mathbf{F} = \mathbf{F}_{\text{surface}} - \sum_{i=1}^{2} \left(\dot{m} \mathbf{V}_{ji} + p_{ji} A_{ji} \mathbf{n}_{ji} \right), \tag{3}$$

where subscripts $i = 1$ and 2 denote injection and suction, respectively; V_j, p_j, and A_j are the mass-averaged jet velocity, pressure, and slot area, respectively; $\mathbf{n}_{ji}$ is the outward unit normal vector of the slot surface.

The aerodynamic coefficients are defined as

$$F_L = \mathbf{F} \cdot \mathbf{y}, \qquad F_D = \mathbf{F} \cdot \mathbf{x}; \tag{4}$$

$$C_L = \frac{F_L}{\frac{1}{2} \rho_\infty V_\infty^2 A_{ref}}, \qquad C_D = \frac{F_D}{\frac{1}{2} \rho_\infty V_\infty^2 A_{ref}}. \tag{5}$$

$C_{L,surface}$ and $C_{D,surface}$ are defined in the same way based on $F_{L,surface}$ and $F_{D,surface}$, respectively.

Time-averaged aerodynamic coefficients are obtained after statistical convergence of the unsteady simulations, i.e., $\langle C_L \rangle$ and $\langle C_D \rangle$. For controlled cases, comparisons between baseline and CFJ configurations are performed using the time-averaged lift and drag coefficients to quantify performance enhancement.

3. Results and Discussion

3.1 Aerodynamic performance

From the engineering perspective, the most important indicator regarding the effects of CFJ is the improvement of force coefficients. **Figure 5** presents the time-averaged force coefficients obtained from URANS simulations for both the baseline configuration and the CFJ-controlled case, including both $\langle C_L \rangle$ and $\langle C_D \rangle$. The calculation accounts for the jet reaction force, as described in Section 2.5.

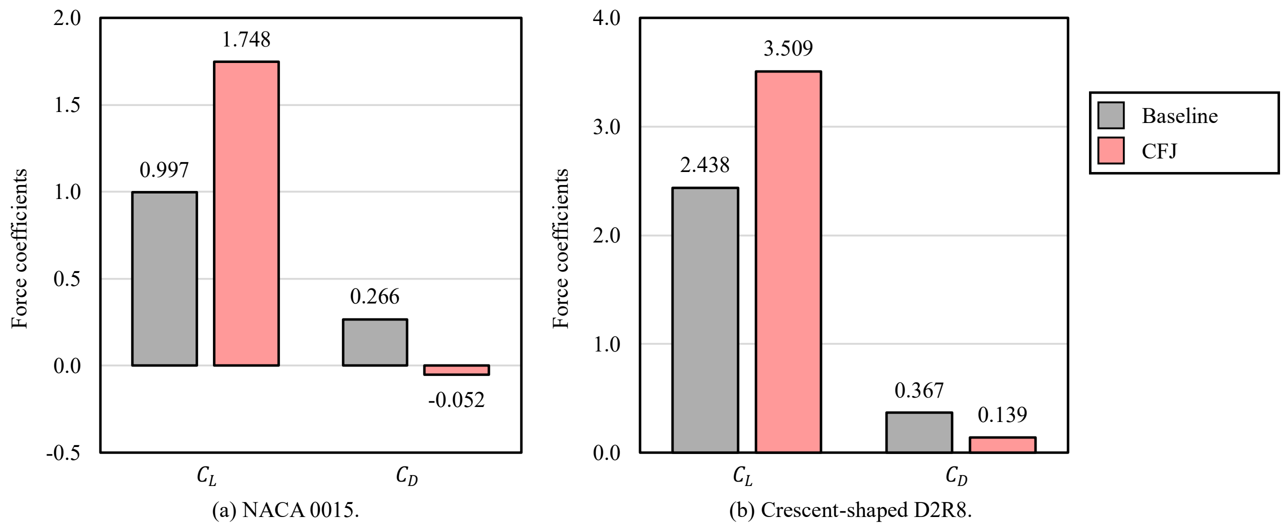

Figure 5. Time-averaged force coefficients.

3.1.1 NACA 0015

For the symmetric NACA 0015 airfoil at $\alpha = 15°$, the baseline case produces $C_L = 0.997$ and $C_D = 0.266$, which is in good agreement with wind tunnel measurements conducted by Sheldahl and Klimas (1981). After CFJ activation, C_L increases to 1.787, corresponding to a 79% enhancement, and the total drag becomes negative ($C_D = -0.052$), indicating net thrust production after accounting for the jet reaction.

Such lift amplification and drag suppression are basically coherent with previously reported CFJ studies on symmetric airfoil sections. For example, two-dimensional CFD investigations on CFJ-equipped airfoils under similar low-to-moderate Re (on the order of 10^5) have shown lift coefficient increases up to 100% relative to baseline when moderate jet momentum coefficients are employed, along with corresponding drag reductions and delayed separation behaviour up to higher angles of attack (Engström *et al.*, 2026a; Vigneswaran & Kumar GC, 2021; Wang *et al.*, 2022; Yazdani *et al.*, 2023).

3.1.2 Crescent-shaped D2R8

The crescent-shaped D2R8 profile exhibits inherently higher baseline lift ($C_L = 2.438$) at $\alpha = 20°$, reflecting its strong camber and aggressive suction-side curvature, which has been documented by a series of previous studies Persson *et al.* (2019); van Reen *et al.* (2025); Zhu *et al.* (2023a); Zhu *et al.* (2023b). The baseline drag ($C_D = 0.367$) is also relatively high, exhibiting a lift-to-drag ratio of 6.6, consistent with the separation-prone nature of this profile near critical incidence.

With CFJ control applied, C_L increases by 44% to 3.509, while C_D decreases by 62% to 0.139. Unlike the symmetric airfoil, drag does not become negative after considering the jet reaction force, but the lift-to-drag ratio improves substantially to 25.2. This trend agrees with previous two-dimensional CFJ investigations on crescent-type wingsails (Engström *et al.*, 2026b), where it was shown that cambered profiles respond differently to momentum injection compared to symmetric sections. In that study, the dominant aerodynamic benefit was not the reversal of drag but rather the stabilization of the suction-side shear layer, which in turn delayed separation onset and promoted improved pressure recovery in the mid-chord region. As a result, the lift enhancement primarily originated from sustained flow attachment and strengthened suction rather than from a fundamental redistribution of the global force balance. In Section 3.2, the flow mechanism is discussed in more detail.

Compared with the two-dimensional simulations, the three-dimensional computations allow the vortical structures to develop in the spanwise direction, including the interaction between separated shear layers (Park *et al.*, 2017; Zhu *et al.*, 2023b). These inherently three-dimensional effects have an influence on the circulation distribution, leading to differences in the predicted lift and drag coefficients relative to the two-dimensional results (Toosi *et al.*, 2024). However, as the present study is based on a finite-aspect-ratio wingsail, it introduces intrinsic three-dimensional effects that influence both the flow separation pattern and the global aerodynamic loads, though this configuration is more representative of practical applications than a two-dimensional section (Toosi *et al.*, 2024). Therefore, it is acknowledged that the results reported herein should be interpreted within the context of a finite-aspect-ratio configuration, and extrapolation to very high aspect ratio or freestream tip conditions should be made with caution.

3.2 Flow mechanisms

This section focuses on the crescent-shaped D2R8 profile, for which the CFJ control leads to substantial lift enhancement and drag reduction, as shown in Section 3.1.2. The objective here is to elucidate the underlying flow mechanisms responsible for these aerodynamic improvements.

3.2.1 Pressure distribution

For analyzing the mechanism causing the differences in force coefficients presented in Section 3.1.2, **Figure 6** presents the pressure coefficient distribution along the midspan section of the D2R8 profile, together with instantaneous pressure contours for the baseline and CFJ-controlled cases.

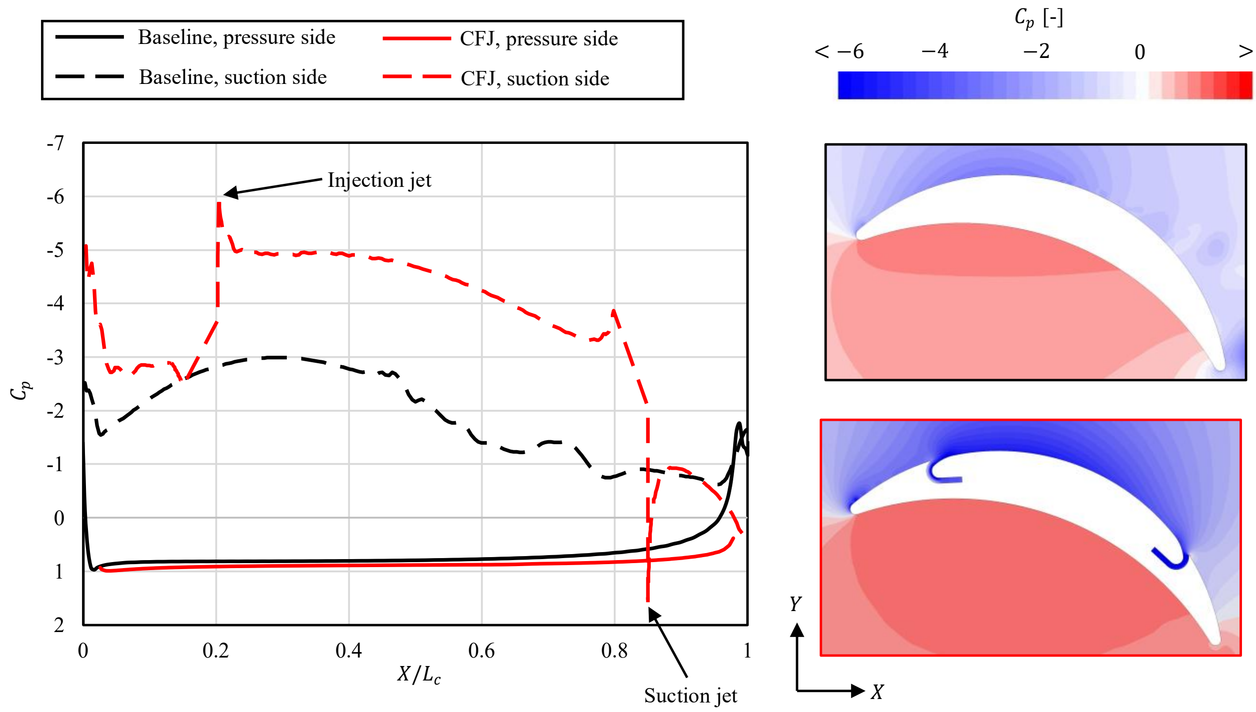

Figure 6. Pressure coefficient along the midspan section. Crescent-shaped D2R8 profile.

In the baseline configuration, the suction-side pressure distribution exhibits a moderate leading-edge suction peak followed by a rapid pressure recovery. Downstream of approximately $X/L_c \approx 0.3$, the suction level weakens significantly, indicating the presence of strong adverse pressure gradients and partial flow separation. This behavior is consistent with the high drag and limited lift increase observed in Section 3.1.2.

With CFJ activated, several distinct modifications in the pressure field can be identified. First, near the injection slot (around $X/L_c \approx 0.2$), a pronounced local suction peak is generated. Previous studies on co-flow jet separation control have similarly reported that leading-edge tangential injection can create a localized low-pressure region by energizing the near-wall flow, which helps the boundary layer overcome the adverse pressure gradient (Xu *et al.*, 2021; Xu & Zha, 2023a). This intensified negative pressure region indicates that the injected momentum enhances near-wall acceleration and strengthens the suction-side circulation. As a result, the leading-edge suction is substantially amplified compared to the baseline case. Next, the suction-side pressure remains significantly lower over a broader chordwise extent, particularly in the mid-chord region. Instead of experiencing rapid pressure recovery as in the baseline case, the CFJ-controlled configuration maintains a more sustained negative pressure distribution. This indicates that the shear layer remains attached over a longer distance, delaying separation onset. Then, near the suction slot (around $X/L_c \approx 0.85$), a sharp pressure variation is observed due to the localized extraction of mass. This suction mechanism removes low-momentum fluid from the boundary layer and modifies the downstream pressure field.

The combined effect of these mechanisms directly explains the aerodynamic trends reported in Section 3.1.2. The sustained low-pressure region along the suction side increases the overall circulation, leading to the observed lift enhancement. Xu and Zha (2023b) also noted that although increased suction contributes to higher lift, the associated adverse pressure gradient can increase pressure drag locally unless compensated by momentum injection. It is important to note that the CFJ-induced low-pressure region in the downstream half of the suction side actually contributes positively to the pressure drag. Compared to the baseline case, the intensified suction near the aft portion increases the streamwise component of the surface pressure force acting opposite to the incoming flow. Therefore, when considering only the external aerodynamic field, the pressure redistribution induced by CFJ does not inherently reduce drag; in fact, it can increase the pressure drag contribution. The observed reduction in C_D in Section 3.1.2 is not a consequence of separation suppression, but is primarily attributed to the jet reaction term introduced in the force correction. The momentum exchange associated with the injection–suction system generates a net thrust component that offsets the increased external pressure drag.

The pressure contour plots in **Figure 6** further explain this interpretation. In the baseline case, the suction-side low-pressure region appears diffused and partially detached from the surface, suggesting separation and recirculation. In contrast, under CFJ control, the low-pressure region remains tightly attached to the surface and extends farther downstream, indicating sustained attachment and enhanced flow coherence.

3.2.2 Flow separation

The streamwise velocity distribution at mid-span reveals a distinct separation region over the downstream half of the suction side in the baseline configuration (**Figure 7**(a)). The shear layer detaches around mid-chord and rolls into a large recirculation bubble extending toward the trailing edge, while the case with CFJ shows different phenomena (**Figure 7**(b)).The flow field provides direct evidence of the separation behavior underlying the pressure redistribution discussed in Section 3.2.1.

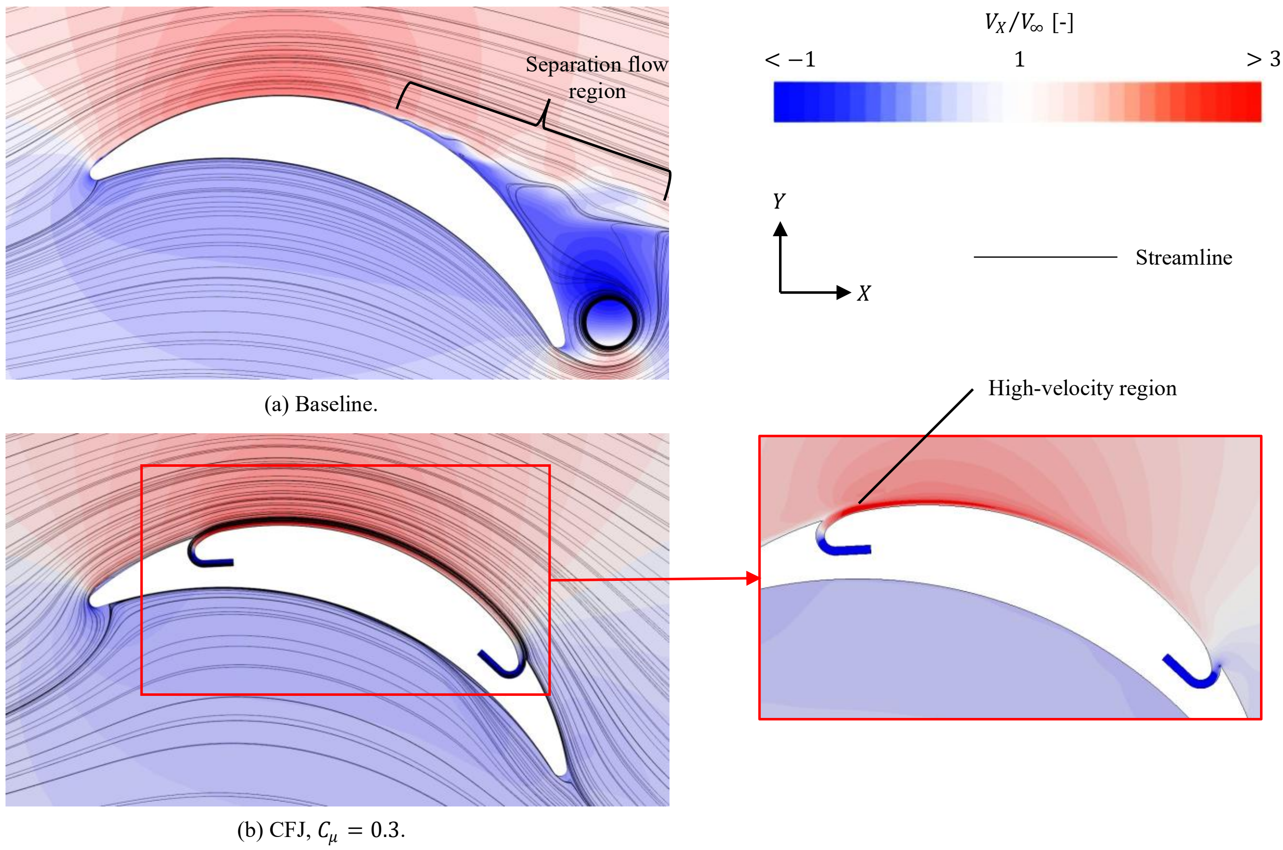

Figure 7. Streamwise velocity distribution and streamlines at the midspan section. Crescent-shaped D2R8 profile.

In the baseline configuration (**Figure 7**(a)), a distinct separation region develops over the downstream half of the suction side. The shear layer detaches around mid-chord and rolls into a large recirculation bubble extending toward the trailing edge. The presence of reversed flow and low-velocity regions indicates significant boundary-layer separation, which is consistent with the pressure recovery observed in Section 3.2.1. Once separation occurs, the suction-side pressure gradient weakens, leading to a loss of suction strength and limiting lift generation. Similar large-scale separated shear layers have been reported for highly cambered wings at moderate Reynolds numbers, where the adverse pressure gradient induces mid-chord detachment followed by vortex roll-up in the wake (Atkinson, 2019; Zeng *et al.*, 2023; Zhu *et al.*, 2024b).

In contrast, with CFJ activated (**Figure 7**(b)), the separation region is substantially suppressed. The injection jet introduces high-momentum fluid along the suction surface, forming a high-velocity layer that remains closely attached to the airfoil wall. This injected near-wall flow prevents detachment of the shear layer and maintains flow attachment over a much larger portion of the chord. The suction jet near the trailing edge further removes low-momentum fluid from the boundary layer, mitigating the accumulation of adverse pressure gradient effects in the downstream region. As a result, the vortex shedding observed in the baseline case disappears, and the streamlines remain attached up to the trailing edge. These flow characteristics directly explain the pressure distribution trends reported in Section 3.2.1, as the sustained attachment of the shear layer allows the suction-side low-pressure region to persist farther downstream, producing the extended negative pressure area in the CFJ case. In addition, it can be explained that the upstream suction peak and the downstream suction valley in **Figure 6** correspond to the locally accelerated flow induced by the injection and suction jet, respectively.

To further analyze the three-dimensional vortical structures in the periodic domain, **Figure 8** shows Q-criterion iso-surfaces of the baseline and CFJ cases. In the spanwise direction, the flow exhibits pronounced three-dimensional structures associated with shear layer instability and spanwise modulation, even in the absence of geometric tips due to the periodic top and bottom boundary conditions. In separated flows, the initial shear layer emanating from the leading edge is susceptible to spanwise deformations as three-dimensional perturbations amplify downstream, forming vortex rollers with significant spanwise variation (Hao *et al.*, 2025; Zhiyin, 2019). In the baseline case, the Q-criterion iso-surfaces highlight elongated vortical formations stretching along the span, indicating strong spanwise fluctuation and interaction among neighboring vortical regions. This variation correlates with unsteady separation and enhanced mixing across the spanwise direction, which contributes to performance degradation through uneven lift distribution and broader shear layer dynamics. With CFJ activation, these spanwise variations are markedly attenuated; the energetic spanwise vortical formations are weakened and localized closer to the separation onset region, reflecting reduced spanwise instability. The spanwise structures observed in the three-dimensional simulations indicate the presence of shear-layer instabilities that redistribute momentum along the span, producing localized variations in attachment and separation.

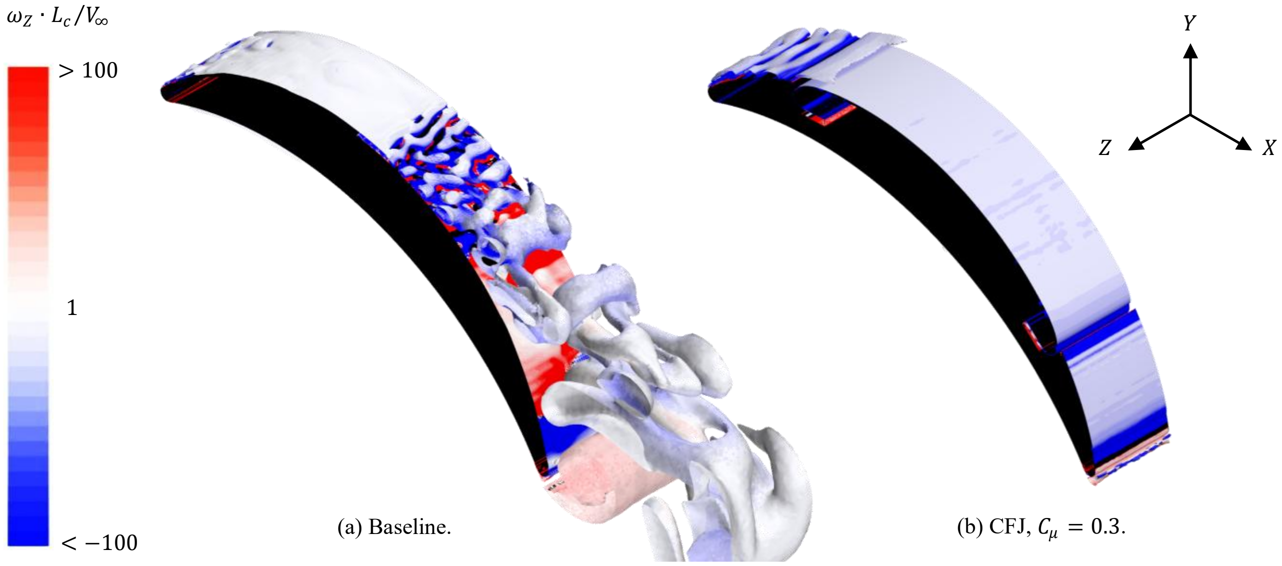

Figure 8. Spanwise vorticity distribution at the iso-surface of $Q = 15 \cdot V_\infty^2 \cdot L_c^{-2}$. Crescent-shaped D2R8 profile.

3.2.3 Laminar–turbulent transition

The turbulence kinetic energy distribution at the midspan section is shown in **Figure 9**. As discussed by Zhu (2024), the flow separation patterns of crescent-shaped profiles are sensitive to Re, which may lead to a so-called “force crisis,” i.e., abrupt changes in lift and drag coefficients occurring at critical Re (Bot *et al.*, 2016). In addition, due to their strong suction-side curvature, crescent-shaped profiles are prone to leading-edge separation bubbles (LESBs) at moderate Reynolds numbers (Re~10^5−10^6) (Souppez *et al.*, 2022; Zhu, 2024), as observed in the baseline case in **Figure 9**(a). It should be noted that according to previous studies (Zhu, 2024), such LESBs are expected to be weakened or suppressed under strongly turbulent atmospheric boundary layer conditions. Since the present study is conducted at model scale, the potential influence of CFJ on laminar–turbulent transition is also briefly examined.

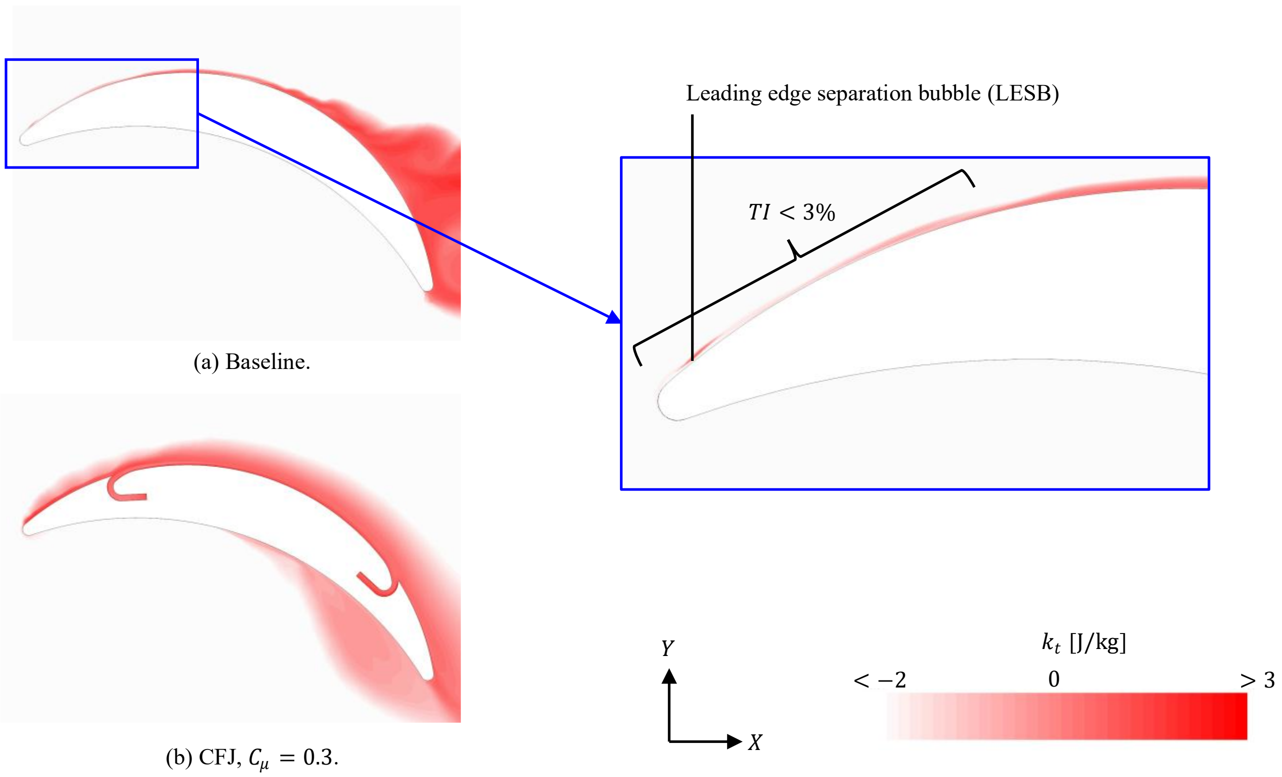

Figure 9. Distribution of turbulence kinetic energy at the midspan section. Crescent-shaped D2R8 profile.

With CFJ activated, turbulence levels increase near the injection location, and the laminar separation bubble is no longer clearly distinguishable. The injected high-momentum flow promotes earlier transition and supports a more robust near-wall turbulent boundary layer. Besides, connected with **Figure 6**, with CFJ activation, the pressure distribution is significantly modified, leading to a stronger leading-edge suction and a shift in the separation topology. Although transition dynamics are not the primary focus of the present study, these results confirm that CFJ modifies not only large-scale separation but also the laminar–turbulent transition characteristics of the crescent profile.

3.3 LES-based flow structure analysis

To further examine the underlying flow structures, an additional LES is performed for the NACA 0015 case with CFJ. The LES simulations employ the wall-adapting local eddy-viscosity (WALE) subgrid-scale model. The same as the URANS method presented in Section 2, the near-wall resolution satisfies $y^+ < 1$, with typical values on the order of 10^{-1}. The inlet flow is prescribed with a turbulence intensity of 6%, without synthetic turbulence generation. A hybrid second-order upwind and bounded central scheme is used for spatial discretization.

The time-averaged lift and drag coefficients obtained from LES differ by less than 2% compared to the URANS results, indicating that the integral aerodynamic loads are well captured by the URANS framework under the present conditions.

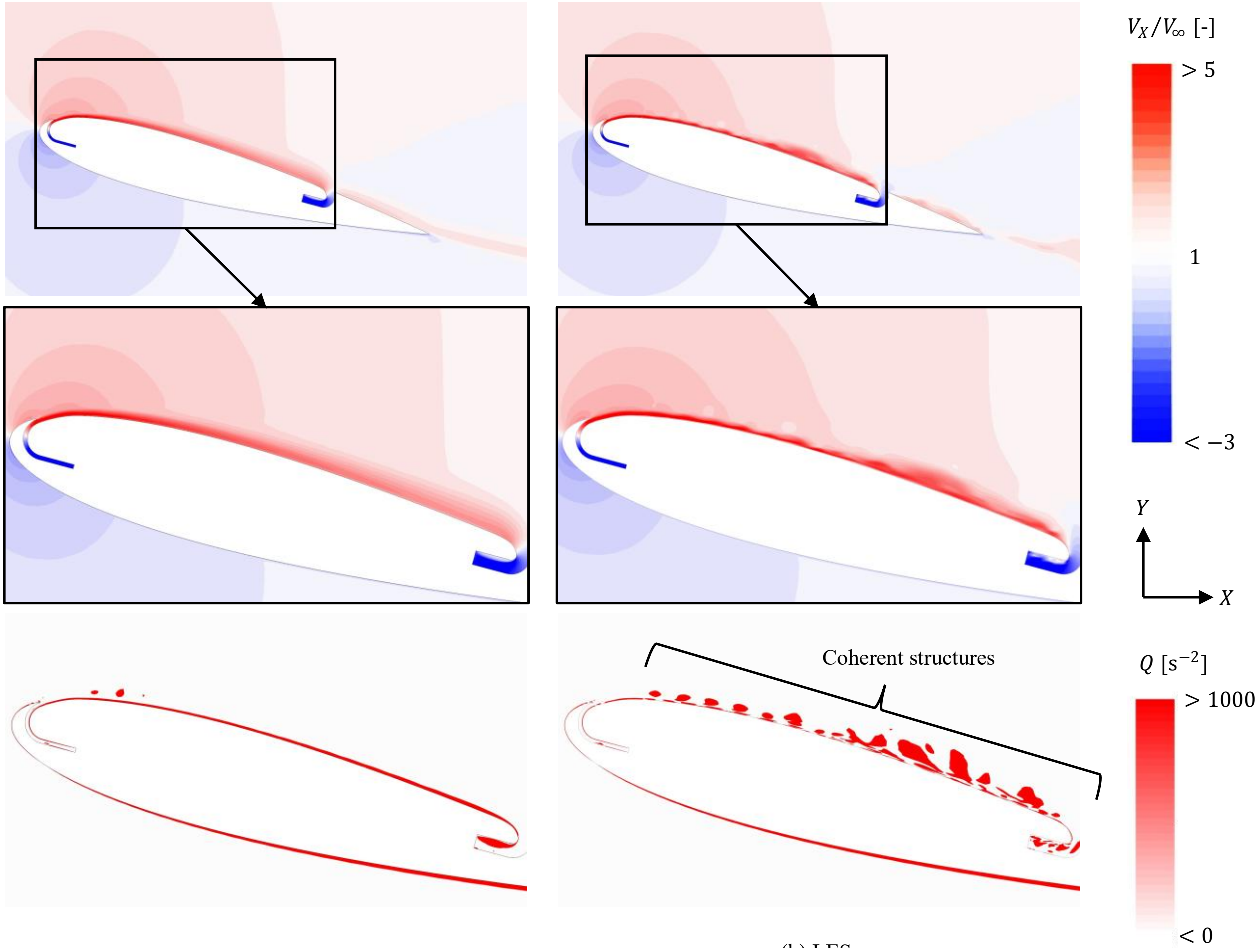

(a) URANS. (b) LES.

Figure 10. Distribution of streamwise velocity and Q-criterion at the midspan section. NACA 0015 profile.

However, the instantaneous flow fields reveal additional complexity. As shown in **Figure 10**, while the URANS solution provides a smooth representation of the separated shear layer, the LES results exhibit pronounced coherent structures developing along the suction-side shear layer. Similar Kelvin–Helmholtz-type vortical structures have been observed in previous high-fidelity numerical or experimental studies of separated shear layers, where the strong velocity gradients trigger shear-layer instability and lead to coherent vortical roll-up patterns not captured by eddy-viscosity RANS models (Im *et al.*, 2011; Lefebvre *et al.*, 2013; Silva & Wolf, 2024). The Q-criterion distribution highlights these organized vortical motions, which originate from the shear layer and convect downstream under the influence of local inflectional instability. Such dynamics are inherently unsteady and cannot be fully resolved within the eddy-viscosity-based URANS formulation. Although these small- to intermediate-scale vortical structures do not significantly alter the time-averaged force coefficients, coherent structures of this type have been linked to force fluctuations and pressure oscillations in other aerodynamic applications and may have implications for unsteady loading and aeroelastic interactions (Lengani & Simoni, 2015; Zhu *et al.*, 2024a).

4. Conclusions

This study presents a three-dimensional numerical investigation of active flow control applied to rigid wingsails, using a CFJ approach, with two sectional profiles: NACA 0015 and crescent-shaped D2R8. The results demonstrate that the introduction of CFJ significantly modifies the flow separation patterns over the suction side, leading to enhanced pressure recovery and delayed stall. Compared with the baseline configuration, the controlled cases exhibit an increase in lift coefficient and a corresponding improvement in thrust generation for the WASP system.

It should be noted that the present study is conducted under controlled inflow conditions at moderate Reynolds numbers, without explicitly accounting for atmospheric boundary layer effects, high free-stream turbulence, or the energy consumption of the active CFJ system. Therefore, the results are primarily intended to provide mechanistic insights into three-dimensional separation control, rather than a direct quantitative assessment of full-scale wingsail performance.

The enhancement in lift can be attributed to the modification of the boundary-layer momentum distribution induced by CFJ. The jet injection energizes the near-wall flow, suppresses or shortens the separation bubble, and stabilizes the shear layer development over the suction surface. As a consequence, the adverse pressure gradient is better sustained, the suction peak is strengthened, and the effective circulation around the wingsail increases. This mechanism is observed for both sectional profiles, although the response differs due to their distinct baseline separation characteristics.

The three-dimensional simulations show that the interaction between the injected jet and the separated shear layer strongly influences the global aerodynamic response. The CFJ not only suppresses large-scale separation but also redistributes circulation along span, thereby altering both sectional and overall force characteristics. This suggests that two-dimensional analyses may misestimate the influence of spanwise flow development on controlled wingsail performance.

Furthermore, the results indicate that URANS simulations cannot fully capture the flow characteristics, e.g., the coherent structures. Future work will employ LES or other high-fidelity approaches to further resolve the unsteady flow structures and to gain deeper insight into the three-dimensional control mechanisms associated with CFJ on cambered wingsails.

ACKNOWLEDGEMENTS

The authors would like to acknowledge the resources provided by Chalmers University of Technology. The computations were enabled by resources provided by the National Academic Infrastructure for Supercomputing in Sweden (NAISS) at Tetralith, partially funded by the Swedish Research Council through grant agreement no. 2022-06725. This work is partially funded by the Swedish Transport Agency under grant TRV 2024/99638. Dr. Kewei Xu acknowledges the start-up funding provided by the Office of the Vice President for Research and Dean of the Graduate School, University of Maine. The authors would also like to thank the Center for Undergraduate Research (CUGR) at the University of Maine.

REFERENCES

Atkinson, G. M. (2019). Analysis of lift, drag and CX polar graph for a 3D segment rigid sail using CFD analysis. *Journal of Marine Engineering and Technology*, *18*(1), 36-45.

Balaji, K., & Wessley, G. J. J. (2023). Studies on the enhancement of aerodynamic performance in aerofoils using co-flow jet: a comprehensive review. *Aerospace Systems*, *6*(1), 1-14.

Bot, P., Rabaud, M., Thomas, G., Lombardi, A., & Lebret, C. (2016). Sharp transition in the lift force of a fluid flowing past nonsymmetrical obstacles: evidence for a lift crisis in the drag crisis regime. *Physical review letters*, *117*(23), 234501.

Cairns, J., Vezza, M., Green, R., & MacVicar, D. (2021). Numerical optimisation of a ship wind-assisted propulsion system using blowing and suction over a range of wind conditions. *Ocean Engineering*, *240*, 109903-109903.

Charrier, B., Constans, J., Cousteau, J.-Y., Daïf, A., Malavard, L., & Quinio, J.-L. (1985). Fondation Cousteau and windship propulsion 1980–1985 system Cousteau-Pechiney. *Journal of Wind Engineering and Industrial Aerodynamics*, *20*(1-3), 39-60.

Ding, F., Jeon, J., & Zha, G. (2025). Simulation of 3D Co-Flow Jet Wings with Circular End-Plates. AIAA AVIATION FORUM AND ASCEND 2025,

Du, X., Chen, J., Guo, L., Wang, Y., Hu, S., Wang, H., & Liu, X. (2026). Experimental aerodynamic investigation of a suction sail model. *Ocean Engineering*, *351*, 124366.

Du, X., Liu, X., Wang, Y., Yu, H., Chen, X., & Chen, J. (2025). Study on the Aerodynamic Performance and Research Methods of Turbosails. ISOPE International Ocean and Polar Engineering Conference,

Engström, P., Friess, L., Xu, K., & Bensow, R. (2026a). High efficiency co-flow jet wingsail airfoil for sustainable maritime transportation. AIAA SCITECH 2026 Forum,

Engström, P., Xu, K., & Bensow, R. (2025). Performance Enhancement of Multiple Wingsail Airfoils Using Co-flow Jet Active Flow Control. AIAA SCITECH 2025 Forum,

Engström, P., Xu, K., & Bensow, R. (2026b). Co-Flow Jet Crescent-Shaped Airfoil for High-Thrust Wind Propulsion. AIAA SCITECH 2026 Forum,

Giovannetti, L. M., Dhome, U., Malmek, K., Persson, A., & Wielgosz, C. (2022). Multi-wing sails interaction effects. SNAME Chesapeake Sailing Yacht Symposium,

Hao, X., He, X., Zhang, Z., & Li, J. (2025). A Review of Simulations and Machine Learning Approaches for Flow Separation Analysis. *Aerospace*, *12*(3), 238.

Ho, H. H., Shirinzad, A., Essel, E. E., & Sullivan, P. E. (2024). Synthetic jet actuators for active flow control: A review. *Fluids*, *9*(12), 290.

Huang, J., & Souppez, J.-B. (2025). State of the Art in Wind Assisted Ship Propulsion for Maritime Decarbonisation and Sustainable Shipping: A Systematic Review. *Journal of Sailing Technology*, *10*(01), 258-278.

Im, H., Zha, G., & Dano, B. (2011). Investigation of co-flow jet airfoil mixing mechanism using large eddy simulation. 41st AIAA Fluid Dynamics Conference and Exhibit,

Jahanmiri, M. (2010). Active flow control: a review. *Chalmers University of Technology*.

Khan, L., Macklin, J., Peck, B., Morton, O., & Souppez, J.-B. R. G. (2021, 2021/9//). A review of wind-assisted ship propulsion for sustainable commercial shipping: Latest developments and future stakes. Proceedings of the Wind Propulsion Conference 2021, London, UK.

Langtry, R. B., & Menter, F. R. (2009). Correlation-based transition modeling for unstructured parallelized computational fluid dynamics codes. *AIAA Journal*, *47*(12), 2894-2906.

Lefebvre, A., Dano, B., Difronzo, M., Bartow, W., & Zha, G. (2013). Performance of a co-flow jet airfoil with variation of Mach number. 51st AIAA Aerospace Sciences Meeting including the New Horizons Forum and Aerospace Exposition,

Lengani, D., & Simoni, D. (2015). Recognition of coherent structures in the boundary layer of a low-pressure-turbine blade for different free-stream turbulence intensity levels. *International Journal of Heat and Fluid Flow*, *54*, 1-13.

Li, D., Li, G., Dai, J., & Li, P. (2017). A new type of collapsible wing sail and its aerodynamic performance. International Conference on Offshore Mechanics and Arctic Engineering,

Lu, R., & Ringsberg, J. W. (2020). Ship energy performance study of three wind-assisted ship propulsion technologies including a parametric study of the Flettner rotor technology. *Ships and Offshore Structures*, *15*(3), 249-258.

Menter, F. R. (1993). Zonal two equation κ-ω turbulence models for aerodynamic flows. AIAA 23rd Fluid Dynamics, Plasmadynamics, and Lasers Conference, Orlando,FL,U.S.A.

Ouchi, K., Uzawa, K., & Kanai, A. (2011). Huge Hard Wing Sails for the Propulsor of Next Generation Sailing Vessel. Second International Symposium on Marine Propulsors, Hamburg, Germany.

Park, J. S., Witherden, F. D., & Vincent, P. E. (2017). High-order implicit large-eddy simulations of flow over a NACA0021 aerofoil. *AIAA Journal*, *55*(7), 2186-2197.

Pasa, J., Alam, M. M., Arumuru, V., Chen, H., & Cheng, T. (2026). Advancements in Synthetic Jet for Flow Control and Heat Transfer: A Comprehensive Review. *Fluids*, *11*(1), 22.

Persson, A., Li, D. Q., Olsson, F., Werner, S., & Dhomé, U. (2019). Performance prediction of wind propulsion systems using 3D CFD and route simulation. RINA, Royal Institution of Naval Architects-International Conference on Wind Propulsion, WP 2019, 15-16 October 2019, London, United Kingdom,

Petković, M., Zubčić, M., Krčum, M., & Pavić, I. (2021). Wind Assisted Ship Propulsion Technologies–Can they Help in Emissions Reduction? *NAŠE MORE: znanstveni časopis za more i pomorstvo*, *68*(2), 102-109.

Ren, Y., Lei, Z., & Zha, G. (2026). High-Thrust Stationary Cylindrical Wind Sails Enabled by CoFlow Jet with Enhanced Tip Treatment. *Journal of Sailing Technology*, *11*(01), 48-69.

Sheldahl, R. E., & Klimas, P. C. (1981). *Aerodynamic characteristics of seven symmetrical airfoil sections through 180-degree angle of attack for use in aerodynamic analysis of vertical axis wind turbines*. http://www.osti.gov/servlets/purl/6548367/

Siemens PLM Software. (2021). STAR-CCM+ user guide (version 16.02). In: Siemens PLM Software Inc: Munich, Germany.

Silva, L. J., & Wolf, W. R. (2024). Embedded shear layers in turbulent boundary layers of a NACA0012 airfoil at high angles of attack. *International Journal of Heat and Fluid Flow*, *107*, 109353.

Souppez, J.-B. R., Bot, P., & Viola, I. M. (2022). Turbulent flow around circular arcs. *Physics of Fluids*, *34*(1).

Souppez, J.-B. R., & Viola, I. M. (2024). Water tunnel testing of downwind yacht sails. *Experiments in Fluids*, *65*(2), 1-19.

Su, Y., Du, H., Deng, R., & Xia, H. (2023). Wind tunnel experimental study of aerodynamic characteristics of co-flow jet wing with built-in air source. *Aerospace science and technology*, *143*, 108712.

Thies, F., & Fakiolas, K. (2022). Wind propulsion. In *Sustainable Energy Systems on Ships* (pp. 353-402). Elsevier.

Toosi, S., Peplinski, A., Schlatter, P., & Vinuesa, R. (2024). The impact of finite span and wing-tip vortices on a turbulent NACA0012 wing. *Journal of Fluid Mechanics*, *997*, A68.

van Reen, S., Serbülent, B., & Yao, H.-D. (2025). Machine learning-based multipoint optimisation for improving aerodynamics of symmetrically cambered wing sails in wind-assisted ship propulsion. *Ocean Engineering*, *342*, 122829.

Vigneswaran, C., & Kumar GC, V. (2021). Aerodynamic performance analysis of co-flow jet airfoil. *International Journal of Aviation, Aeronautics, and Aerospace*, *8*(1), 10.

Wang, R., Zhang, G., Ying, P., & Ma, X. (2022). Effects of key parameters on airfoil aerodynamics using co-flow jet active flow control. *Aerospace*, *9*(11), 649.

Workinn, D. (2021). *A high-level interface for a sailing vessel* http://urn.kb.se/resolve?urn=urn:nbn:se:kth:diva-299430

Xu, K., Malmek, K., & Bensow, R. (2025). Numerical investigation of multiple wingsails interaction under different apparent wind angles. *Ocean Engineering*, *336*, 121712.

Xu, K., Ren, Y., & Zha, G. (2021). Separation control by co-flow wall jet. AIAA AVIATION 2021 FORUM,

Xu, K., & Zha, G. (2021). High control authority three-dimensional aircraft control surfaces using coflow jet. *Journal of Aircraft*, *58*(1), 72-84.

Xu, K., & Zha, G. (2023a). Enhancing aircraft control surface effectiveness by co-flow jet flap at low energy expenditure. *Aerospace science and technology*, *133*, 108145.

Xu, K., & Zha, G. (2023b). Separation control and the energy expenditure using pulsed co-flow jet. AIAA Scitech 2023 Forum,

Yazdani, S., Salimipour, E., Salimipour, A., Sheremet, M. A., & Ghalambaz, M. (2023). Effects of coflow-jet active flow control on airfoil stall. *International Journal of Numerical Methods for Heat & Fluid Flow*, *33*(6), 2278-2294.

Zeng, Q., Cai, W., & Xu, J. (2024a). Large-Eddy Simulation of Low-Frequency Flow Oscillations for NACA0012 and Dynarig Sail at Large Attack Angles. *Journal of marine science and engineering*, *12*(5), 835.

Zeng, Q., Lyu, X., Cai, W., Zhang, L., & Xu, J. (2024b). Influence of wind gradient and ground effect on the aerodynamic forces of a Dynarig sail at large heeling angles. *Ocean Engineering*, *312*, 119069.

Zeng, Q., Zhang, X., Cai, W., & Zhou, Y. (2023). Wake distortion analysis of a Dynarig and its application in a sail array design. *Ocean Engineering*, *278*, 114341.

Zha, G.-C., Gao, W., & Paxton, C. D. (2007). Jet effects on coflow jet airfoil performance. *AIAA Journal*, *45*(6), 1222-1231.

Zhang, H., Hu, Y., & He, J. (2022). Wind tunnel experiment of multi-mode arc sail device. *Polish Maritime Research*, *28*(4), 20-29.

Zhang, R., Huang, L., Ma, R., Peng, G., Ruan, Z., Wang, C., Zhao, H., Li, B., & Wang, K. (2024). Numerical investigation on the effects of heel on the aerodynamic performance of wing sails. *Ocean Engineering*, *305*, 117897.

Zhiyin, Y. (2019). Secondary instability of separated shear layers. *Chinese Journal of Aeronautics*, *32*(1), 37-44.

Zhu, H. (2024). *Analysis and evaluation of wingsails with crescent-shaped profiles: from aerodynamics to aeroelasticity* Chalmers University of Technology]. Gothenburg, Sweden.

Zhu, H., Chernoray, V., Yao, H.-D., Ringsberg, J. W., & Ramne, B. (2023a). Experimental study on structure responses of triple wing sails to turbulence flows at multiple apparent wind angles. 9th International Conference on Marine Structures , MarStruct, Gothenburg, Sweden.

Zhu, H., Chernoray, V., Yao, H.-D., Ringsberg, J. W., & Ramne, B. (2024a). Fluid-structure interaction analysis of crescent-shaped wingsails. Proceedings of the International Conference on Offshore Mechanics and Arctic Engineering - OMAE, Singapore, Singapore.

Zhu, H., Yao, H.-D., & Ringsberg, J. W. (2024b). Unsteady RANS and IDDES studies on a telescopic crescent-shaped wingsail. *Ships and Offshore Structures*, 1-14.

Zhu, H., Yao, H.-D., Thies, F., Ringsberg, J. W., & Ramne, B. (2023b). Propulsive performance of a rigid wingsail with crescent-shaped profiles. *Ocean Engineering*, *285*, 115349.